

Deep-Learning Denoising of Radio Observations for Ultra-High-Energy Cosmic-Ray Detection

Zhisen Lai , ^{1,*} Oscar Macias , ^{1,2,†} Aurélien Benoit-Lévy, ³ Arsène Ferrière, ^{3,4} and Matías Tueros , ^{5,6}

¹Department of Physics and Astronomy, San Francisco State University, San Francisco, CA 94132, USA

²GRAPPA – Gravitational and Astroparticle Physics Amsterdam,

University of Amsterdam, Science Park 904, 1098 XH Amsterdam, The Netherlands

³Université Paris-Saclay, CEA, List, F-91120, Palaiseau, France

⁴Sorbonne Université, CNRS, Laboratoire de Physique Nucléaire et des Hautes Energies (LPNHE), 4 Pl. Jussieu, Paris, 75005, France

⁵Instituto de Física La Plata - CCT La Plata - CONICET-UNLP, Diag 113 y 63, La Plata (1900), Argentina

⁶Depto. de Física, Fac. de Cs. Ex., Universidad Nacional de La Plata,
Casilla de Correo 67, La Plata (1900), Argentina

(Dated: February 4, 2026)

Ultra-high-energy cosmic rays (UHECRs) can be detected via the broadband radio pulses produced by their extensive air showers. The Giant Radio Array for Neutrino Detection (GRAND) is a planned radio observatory that aims to deploy autonomous antenna arrays over areas of order $\sim 10^5 \text{ km}^2$ to detect this emission. However, Galactic and instrumental radio backgrounds make the identification of low signal-to-noise ratio (SNR) pulses a central challenge. Here, we present a deep convolutional denoiser model that jointly processes each GRAND antenna trace in the time and frequency domains, allowing the network to learn transient pulse morphology and broadband spectral features while suppressing background noise. By training the model on 4.1×10^5 simulated traces that include detailed UHECR radio emission and realistic detector response and noise, we find a median output-SNR improvement of $\sim 15\text{--}23 \text{ dB}$ in the $50\text{--}200 \text{ MHz}$ band and a reduction of the normalized mean squared error of the waveform by about an order of magnitude relative to a Hilbert-envelope denoiser baseline. We also verify that applying the denoiser to noise-only windows does not produce spurious pulse candidates. Near the detection threshold, the denoiser increases the number of antennas contributing reliable pulse timing by a factor of $\sim 2\text{--}3$, which correspondingly tightens direction reconstruction uncertainties. When we additionally require accurate recovery of the waveform shape, the denoiser yields a median gain of $\sim 3\text{--}4$ antennas usable for energy reconstruction at $\text{SNR} \simeq 5\text{--}6$, strengthening event-level direction and energy estimates in sparse radio arrays.

I. INTRODUCTION

Ultra-high-energy cosmic rays (UHECRs) are extremely rare, so detecting them requires instruments with enormous exposure [1–3]. Large radio antenna arrays, such as the planned Giant Radio Array for Neutrino Detection (GRAND), offer a practical, low-cost way to instrument vast areas for UHECR and neutrino detection [4]. In these experiments, an inclined UHECR air shower produces a nanosecond-scale radio burst in the tens of MHz band, which distant antennas must capture amidst overwhelming ambient and instrumental noise.

Galactic background radiation and human-made radio-frequency interference (RFI) dominate the noise floor at most sites, often masking the faint cosmic-ray pulses [5, 6]. This noise imposes high detection thresholds, which limit the achievable duty cycle and sensitivity of radio UHECR observatories. The central challenge is therefore to extract the short cosmic-ray signal from contaminated waveforms, improving the effective signal-to-noise ratio (SNR) and lowering the threshold for detection.

A variety of classical filtering techniques have been explored in the literature to address this problem. In particular, matched filtering [7] with an expected pulse template can boost sensitivity under idealized (e.g., white-noise) conditions, and it has been shown to reduce trigger thresholds in simulations. However, performance deteriorates significantly under realistic non-Gaussian noise conditions, as RFI does not conform to idealized random background assumptions.

Wavelet-based denoising methods [8], which isolate transient pulses at multiple scales, have proven effective primarily against narrow-band interference and Gaussian noise. Moreover, iterative subtraction algorithms inspired by the radio-astronomy CLEAN [9] approach have been used to remove identifiable interference, in combination with beamforming, in early digital radio detectors [10]. Despite these efforts, conventional methods face limitations. Specifically, they require strong signal models or yield suboptimal results when confronted with complex, non-stationary noise sources. In practice, stringent cuts (e.g., a high SNR threshold after filtering) are often needed to ensure data quality, at the cost of missing weaker UHECR air showers [11].

In the last few years, machine-learning methods have started to remove long-standing sensitivity barriers [12–15]. In particular, convolutional neural networks trained

* zlai@sfsu.edu

† macias@sfsu.edu

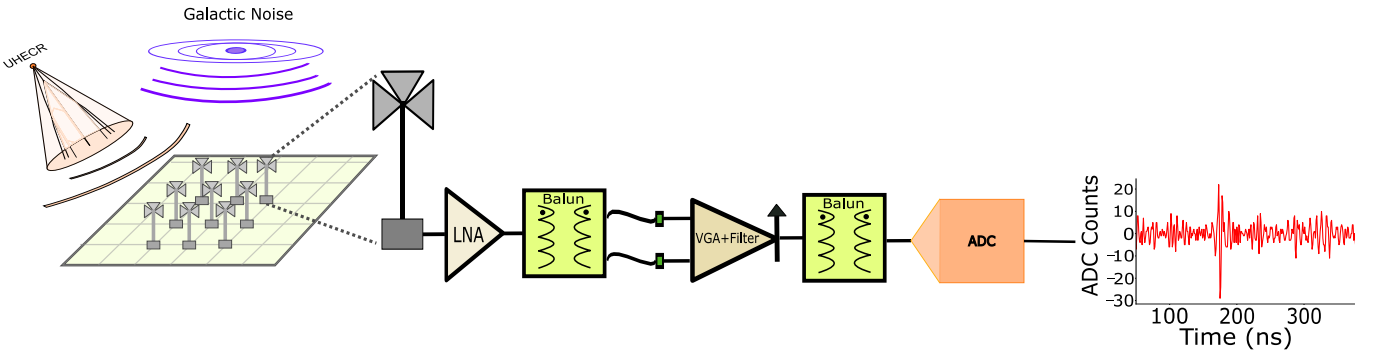


FIG. 1. **Overview of the mock noisy signal generation.** An UHECR air shower produces a short radio pulse that is measured by the GRAND HORIZON antennas [4], whose response we model with a toy model. The incident field is converted to an open-circuit voltage at the antenna, then passed through the analog front end (Low-Noise Amplifier, balun, filter, balun) before digitization by the analog-to-digital counts (ADC) converter. This yields the observed ADC traces which are already embedded in Galactic and instrumental noise. We use these simulated noisy traces to train and validate our ML denoiser model.

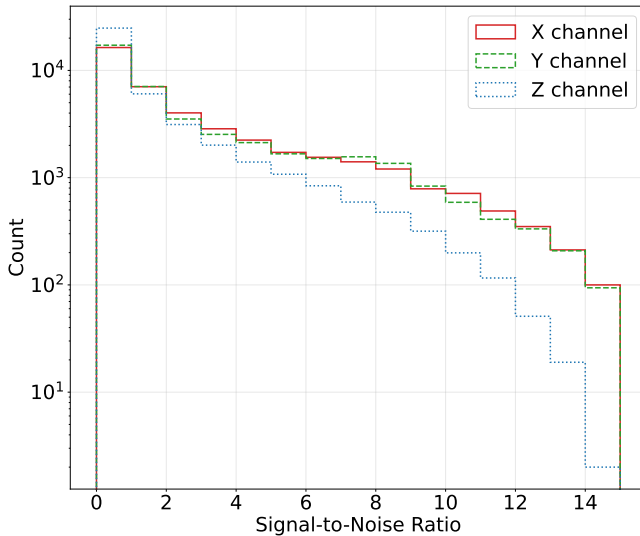


FIG. 2. **Signal-to-Noise Ratio (SNR) distribution of the held-out test sample.** Histogram of the simulated UHECR radio signals as measured by GRAND-like antennas in the three polarization channels (X, Y, Z).

as denoising auto-encoders learn the statistical fingerprints of radio-pulse air-shower signals and retrieve them from noisy traces. Pioneering studies [16–19] demonstrated that a deep CNN autoencoder could both detect the presence of a cosmic-ray pulse and reconstruct its “clean” waveform by removing noise distortions. For example, Ref. [16] used a CNN to successfully retrieve UHECR radio signals from simulated data, achieving on the order of 20% resolution in the reconstructed pulse energy (with no bias) and effectively cleaning out narrow-

band RFI from the signal spectrum. Similarly, the Tunka-Rex Collaboration [17] later showed on measured data that such an autoencoder outperformed standard methods, lowering the detection threshold and retaining accurate shower parameters. Notably, a recent IceCube study [19] applied CNN denoisers to months of recorded data and found about five times more events than a traditional high-threshold trigger, all while improving purity and maintaining the array’s angular resolution. These results underscore that deep learning can recover weak radio pulses that conventional filters would miss, enhancing timing and amplitude fidelity in the reconstructed signals.

In this work, we present a denoising auto-encoder tailored to UHECR radio waveforms, which builds upon these advances (see Ref. [20] for a proceedings article about our early results). Our model is a deep convolutional autoencoder that uses both time-domain and frequency-domain representations of the waveform. By providing the network with a joint view of the raw trace and its frequency content, we enable it to learn informative features of genuine air-shower pulses (such as their characteristic short-lived pulse and broad power spectrum) while recognizing and suppressing various noise patterns. The autoencoder is trained on simulated GRAND-like waveforms, using idealized noise conditions and signal templates generated with established air-shower radio simulations. In training, the network receives a noisy antenna trace as input and is tasked with outputting the denoised electric-field signal; through this process it learns an internal representation of the pulse in both time and frequency that generalizes to signals buried in noise.

Although RFI and other non-stationary backgrounds constitute a central experimental challenge for au-

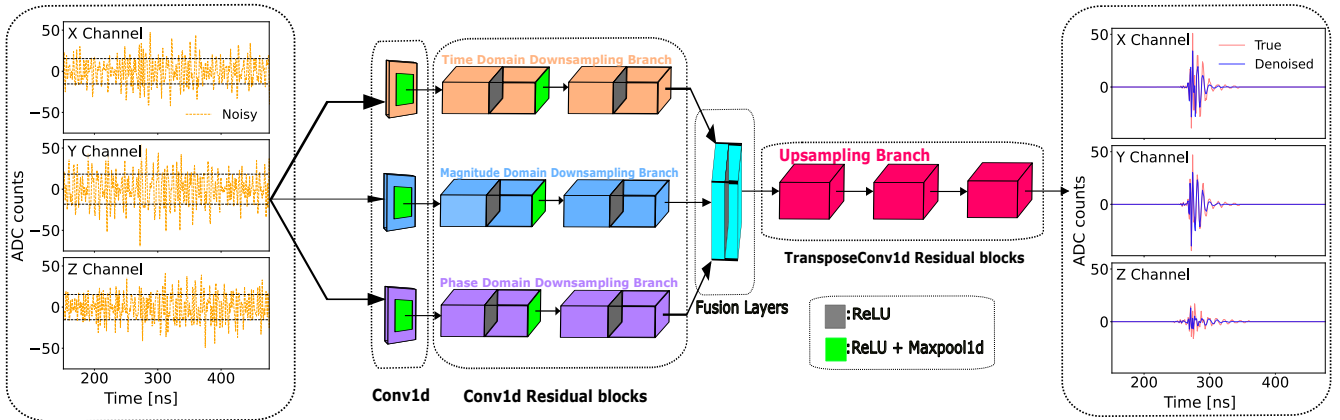


FIG. 3. **Encoder decoder denoiser architecture.** The input consists of three channels sampled in time (with 1,024 bins per channel). The encoder has a time domain branch (orange blocks) and a frequency domain branch that splits into magnitude (dark blue) and phase (purple). Each branch starts with a one dimensional convolution followed by two residual blocks. Their outputs are combined in a fusion module (cyan) that provides a shared latent representation of the time, magnitude, and phase features and uses two additional convolutional layers. The decoder (red blocks) maps this latent representation back to waveform space and returns denoised traces with the same dimensions as the noisy input.

tonomous radio detection, they are actively being mitigated in GRAND through dedicated self-trigger and background-rejection algorithms developed within the NUTRIG program [21, 22]. In this paper we focus on the complementary problem of offline denoising for candidate air-shower traces, isolating the impact of the detector response (RF chain) and a stationary background model on pulse timing and waveform fidelity.

We demonstrate that our proposed denoiser substantially improves the quality of UHECR signal reconstruction. Quantitatively, it yields higher SNR and more accurate pulse timing and amplitude recovery than the Hilbert-envelope denoiser method (adopted in many studies), especially in the low-SNR regime relevant for the weakest air showers. By recovering sub-threshold pulses at individual antennas, the method effectively increases the number of detectors contributing to each event and refines the timestamp alignment across the array, sharpening the reconstructed properties of the UHECRs.

We structure the paper as follows. In Section II we detail the data generation process. Section III presents our denoiser architecture, defines the key performance metrics, and outlines the training schedule. Our results are presented in Section IV. Finally, in Section V we discuss our results, and Section VI summarizes our findings.

II. TRAINING DATASET ASSEMBLY AND PREPROCESSING

A. Air-shower and radio-emission simulations

We simulate the intrinsic radio emission of extensive air showers using the ZHAIRES [23, 24] code. These wave-

forms define our “clean” reference signal at the antenna positions, prior to applying the detector response and adding background noise (described below). The event set consists of downward-going air showers induced by proton and iron primaries, with energies in the range 0.4–4 EeV. Showers are generated over $37^\circ \leq \theta \leq 87^\circ$ with uniform azimuthal coverage (0° – 360°), using the *GRANDProto300* [25] site configuration for the geomagnetic field and atmospheric profile. ZHAIRES outputs the full time-domain vector electric field at each observer position, which we use as the “clean” input throughout this work.

B. Galactic and Instrumental Noise Model

Each GRAND-like detection unit passes its antenna signal through an analog radio-frequency (RF) chain consisting of amplifiers, cables, filters, and digitization electronics [26]. The antenna’s open-circuit voltage is first boosted by a low-noise amplifier (LNA), then sent through coaxial cables and a variable-gain amplifier (VGA), and finally band-limited by analog filters before being sampled by a high-speed ADC [26]. This “RF chain” defines a frequency-dependent transfer function that modifies the incoming radio pulse and introduces a fixed time delay (on the order of tens of nanoseconds) due to signal propagation through the electronics. In addition to shaping the signal, the detector chain adds stochastic noise. A strong source of noise is the diffuse Galactic radio background, which induces voltages in the antenna on the same order as typical air-shower signals [26]. Accordingly, our signal simulation model adds Galactic noise to the shower signal before applying the “RF chain” response (Cf. Fig. 1).

For our training dataset, we emulate these instrumental effects with a simplified “toy” RF chain model. Specifically, we convolve each simulated **ZHAireS** [23, 24] waveform with an approximate transfer function to mimic the net LNA+cable+filter response, thereby reproducing the qualitative frequency filtering and amplification of the real hardware (implemented as a fixed, phenomenological bandpass+gain response, rather than the full component-level RF-chain model in **GRANDLib** [26]).

We also introduce a small random time offset (GPS timing jitter) of a few nanoseconds to each trace, consistent with the timing resolution of GPS-synchronized stations. Finally, we superimpose additive broadband Gaussian noise at a level comparable to the expected Galactic noise floor. Notice that although this simplified prescription does not capture the full local-sidereal-time dependence and spectral coloring of the Galactic background, it suffices to reproduce the overall signal-to-noise regime relevant for training.

In compact form, the simulated voltage trace can be written as

$$v(t) = \mathcal{R}\{v_{\text{sig}}(t - \delta t) + n(t)\}, \quad (1)$$

where \mathcal{R} denotes the toy RF-chain response, δt is the per-trace GPS timing jitter, and $n(t)$ is the additive noise process.

Note that while our toy “RF chain” is not identical to the official GRAND electronics in a quantitative sense, it produces a noisy and band-limited output that is qualitatively similar in its band-limiting and amplification behavior to the official “RF chain” model introduced in **GRANDLib** [26].

C. Training Dataset Construction

We utilize simulated time-series data representative of UHECR events observed by the GRAND detector. Each event consists of three polarized antenna channel traces (X, Y, Z) sampled in 1,024 time bins of 0.5 ns each. To train our denoising model, we utilize paired clean and noisy signals (described in Sec. II B). Our total dataset comprises 410,673 multi-channel traces. We split this into 80% training, 10% validation (used in hyperparameter tuning), and 10% held-out for testing. The clean target signals $X(t)$ are taken from simulated GRAND traces, and the noisy inputs $\hat{X}(t)$ are formed by convolving the clean signal with our toy “RF chain” model. During training, the autoencoder learns to map $\hat{X}(t)$ to $X(t)$ by minimizing the reconstruction error.

Using this pipeline, we construct paired noisy and clean traces spanning a broad range in SNR. Figure 2 summarizes the SNR distribution of the held-out test set used to evaluate the denoiser. Notably, the distribution is intentionally dominated by low-SNR examples, reflecting the operating regime of GRAND-like radio detection where persistent backgrounds (including Galactic and instrumental noise) control near-threshold performance. In

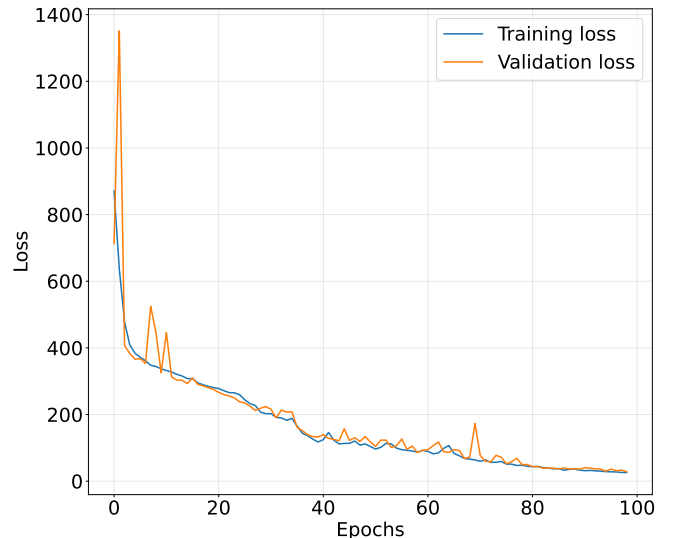


FIG. 4. Evolution of training diagnostics for the best performing hyperparameter configurations. The training and validation losses decline and then level off as the denoising network converges.

TABLE I. Best-performing denoiser hyperparameters selected via **Ray Tune**. These include the encoder/decoder channel widths, and relative magnitude/phase loss weights for the frequency branch of the model (Cf. Fig. 3).

Parameter	Search Space
Criterion	L1
First Conv Channels (Time)	128
Residual Channels (Time)	(128, 256)
First Conv Channels (Mag, Phase)	64
Residual Channels (Mag, Phase)	(128, 256)
Decoder Channels	(32, 16, 8, 3)
Magnitude Weight	0.851123
Phase Weight	0.4351633

this low-SNR domain, signal noise readily translates into biased trigger-time estimates, distorted band-limited amplitudes, and a reduced number of triggered antennas. In contrast, at high SNR the pulse is already clearly distinguishable and conventional linear filtering or template-based methods are typically adequate for stable timing and amplitude reconstruction. The test-set distribution in Fig. 2 therefore targets our regime of interest, where improving reconstruction quality can effectively lower the detection threshold and increase the number of antennas with useful information per event.

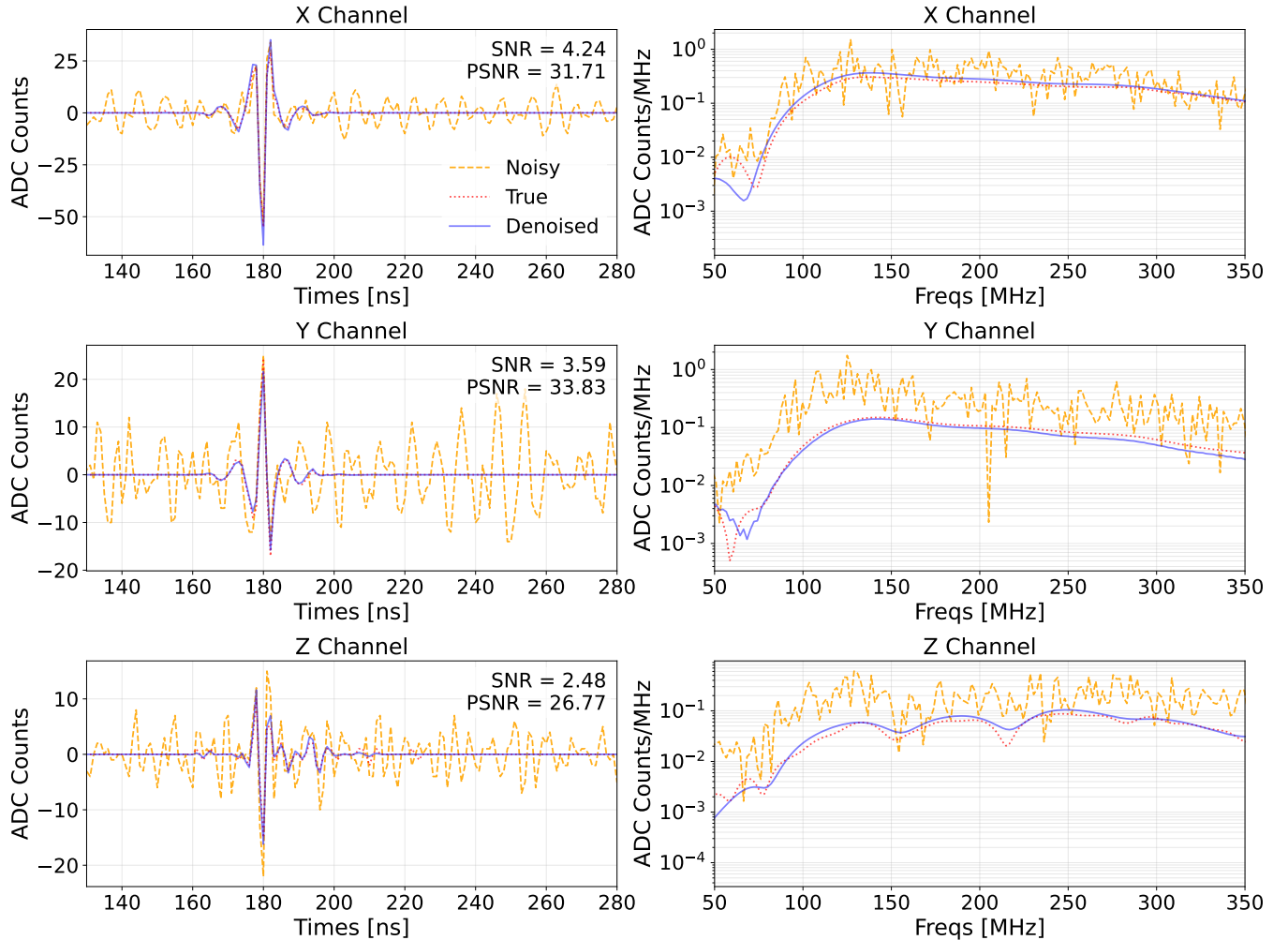


FIG. 5. **Representative denoising reconstructions across channels in the time and frequency domains.** Example three-channel traces (X, Y, Z) for different antenna traces, illustrating a high-SNR case (X; top), an intermediate-SNR case (Y; middle), and a lower-SNR case (Z; bottom). Left panels show the time-domain waveforms: the clean target waveform is shown in red (dotted), the noisy input in orange (dashed), and the denoised reconstruction in blue (continuous). Right panels show the corresponding frequency-domain amplitude spectra (magnitude of the Fourier transform) for the same traces. The per-channel SNR (and PSNR) values are annotated in each time-domain panel.

III. MACHINE-LEARNING DENOISER MODEL AND TRAINING PROCEDURE

A. Denoiser architecture

The denoiser architecture is sketched in Fig. 3. Specifically, we use a dual-branch autoencoder [27] that processes the three polarization traces jointly. One branch operates directly in the time domain to capture localized pulse morphology, while the second branch analyzes the same trace in the frequency domain using real-FFT features represented by the magnitude and phase of the signal. To mitigate edge-driven spectral leakage in the Fourier representation, we apply a Hann taper prior to computing the FFT.

As shown in Fig. 3, each branch follows a structure con-

sisting of a stem 1D convolution, two residual blocks [28], and max pooling after each stage. Three pooling steps compress the temporal axis, yielding compact feature maps in the time and frequency pathways. We then fuse both branches by channel concatenation to form a shared latent code that mixes transient structure with spectral content. Finally, a (three-stage) transposed-convolution decoder inverts the compression and returns the denoised waveform in all three polarizations. The specific channel widths and decoder schedule used throughout this work are listed in Table I; additional technical details are given in Appendix A. The public code release is archived on Zenodo (DOI: [10.5281/zenodo.18233878](https://doi.org/10.5281/zenodo.18233878)) and mirrored on GitHub ([grand-mother/ML_denoising](https://github.com/grand-mother/ML_denoising)).

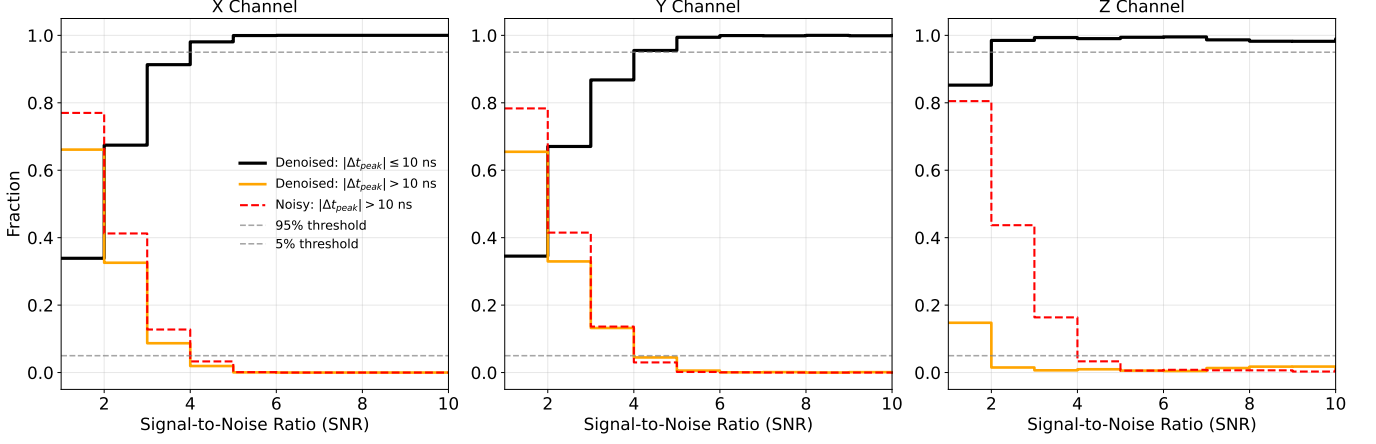


FIG. 6. **Timing reconstruction performance versus SNR.** For each polarization channel (X, Y, and Z), the black curve shows the denoising efficiency $\varepsilon(10 \text{ ns})$, i.e., the fraction of traces whose denoised trigger time agrees with the clean trigger time within 10 ns. The complementary curves indicate the fraction of the same traces with $|\Delta t_{\text{peak}}| > 10 \text{ ns}$ for the denoised output (orange continuous line) and for the standard trigger time estimate from the noisy waveform (red dashed line). Gray dashed lines mark the 95% and 5% reference levels.

B. Training objective

We train the fiducial model with a multi domain L_1 objective that enforces consistency in time and Fourier space. The time domain term (with N samples per channel) is given by

$$L_{\text{time}} = \frac{1}{N} \sum_t |X(t) - \hat{X}(t)|, \quad (2)$$

where the clean and noisy signals are represented by $X(t)$ and $\hat{X}(t)$, respectively.

Furthermore, we compute one sided real FFTs along the time axis as

$$\tilde{X}(f) = \text{RFFT}[X(t)], \quad \tilde{\hat{X}}(f) = \text{RFFT}[\hat{X}(t)], \quad (3)$$

and define magnitude and phase losses as

$$L_{\text{mag}} = \frac{1}{N_f} \sum_f \left| \tilde{X}(f) \right| - \left| \tilde{\hat{X}}(f) \right|, \quad (4)$$

$$L_{\text{phase}} = \frac{1}{N_f} \sum_f \left| \arg \tilde{X}(f) - \arg \tilde{\hat{X}}(f) \right|. \quad (5)$$

The full loss is

$$L_{\text{multi}} = L_{\text{time}} + \sigma_{\text{mag}} L_{\text{mag}} + \sigma_{\text{phase}} L_{\text{phase}}, \quad (6)$$

where σ_{mag} and σ_{phase} weight the magnitude and phase terms and are treated as hyperparameters.

We also explored alternative objectives (e.g., time only losses, multi domain MSE variants, and a PSNR based objective) as ablations. Note that we use Eq. 6 for our baseline results and summarize the objective function comparisons in Appendix B.

C. Performance metrics

We assess denoising performance with two complementary metrics: the *mean-squared error* (MSE), which measures average waveform distortion, and the *peak signal-to-noise ratio* (PSNR), which expresses the same error on a logarithmic scale relative to the peak pulse amplitude. For each trace, we compute

$$\text{MSE} = \frac{1}{N} \sum_t [X(t) - \hat{X}(t)]^2, \quad (7)$$

where N is the number of samples and t indexes the waveform. We then define

$$\text{PSNR} = 10 \log_{10} \left(\frac{A_{\text{max}}^2}{\text{MSE}} \right), \quad A_{\text{max}} = \max_t |\mathcal{H}[X(t)]|, \quad (8)$$

with A_{max} taken as the peak of the analytic-signal envelope. Here $\mathcal{H}[\cdot]$ denotes the Hilbert-transform construction used to obtain the envelope magnitude, providing a robust peak-amplitude proxy for impulsive radio signals.

To quantify the strength of the simulated signals, we compute the *signal-to-noise ratio* (SNR) for each contaminated trace. This is obtained as the peak-envelope amplitude divided by the noise root-mean-square (RMS). In practice, we use

$$\text{SNR} = \frac{\max_t |\mathcal{H}[X(t)]|}{\text{Std}[\hat{X}(t)]}, \quad (9)$$

where $\text{Std}[\cdot]$ is the sample standard deviation. This definition provides a single scalar that tracks how far above background the pulse peak lies, and it is therefore well suited for characterizing the performance of our denoiser model.

D. Optimization, tuning, and data splits

We train and evaluate the denoiser model on the noisy and clean datasets described in Sec. II. The full sample comprises 410,673 traces, split into 80% training, 10% validation, and 10% test. The model selection procedure is performed exclusively on the validation split, and the test set is held out and accessed only once for the final performance analysis.

The network is implemented in PyTorch [29] and optimized with Adam with weight decay [30]. To stabilize training across the broad dynamic range of SNR, we clip the gradient norm at 5. We adopt a cyclical learning-rate schedule [31], treating the lower and upper learning-rate bounds as tunable hyperparameters.

The hyperparameter optimization is carried out with Ray Tune [32] using the Asynchronous Successive Halving Algorithm (ASHA) scheduler [33] to allocate compute efficiently by terminating underperforming trials early. The search spans encoder/decoder widths, batch size, weight decay, cyclical learning-rate bounds, and the spectral loss weights shown in Eq. 6. Furthermore, we select the configuration with the lowest validation loss, and evaluate once on the held-out test set. Training curves for the final configuration are shown in Fig. 4, the adopted hyperparameters are summarized in Table I, and the full Ray Tune hyperparameter setup is given in Tab. II included in the appendix.

IV. RESULTS

Our objective is not merely to recover trigger timing for UHECR direction fitting (e.g., Refs. [34, 35]), but also to reconstruct waveforms with sufficient fidelity so as to extract energy-sensitive observables. We therefore benchmark the denoiser using two complementary criteria: (i) timing and amplitude accuracy (the primary inputs to direction and energy estimators), and (ii) an operational *usable-antenna* criterion that requires spectral-shape consistency within the analysis band. In standard radio reconstructions, antennas are typically included only if a pulse candidate exceeds an SNR threshold (to control noise-induced false positives). Accordingly, this third metric connects denoising directly to reconstruction performance through the effective number of antennas retained per event.

The results presented below are for the fiducial denoiser model described in Sec. III; additional ablation studies are deferred to the Appendix. Figure 5 illustrates representative examples (in the three channels) spanning a range of low to medium SNRs, shown in both the time (left) and frequency (right) domains. As can be seen, at $\text{SNR} \simeq 4.3$ the network approaches an identity map, preserving the pulse morphology and amplitude scale while suppressing small incoherent baseline fluctuations. At $\text{SNR} \simeq 2.5$ the denoiser preferentially removes broadband noise and recovers a compact pulse consistent with the

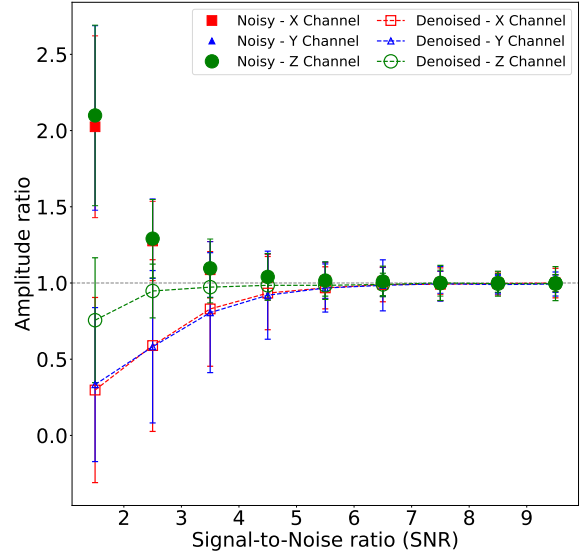


FIG. 7. Peak-amplitude ratio (relative to the injected truth) versus SNR for the X (red), Y (blue), and Z (green) polarization channels. Denoised and noisy estimates are shown with open and filled markers, respectively. The dashed horizontal line indicates a perfect amplitude ratio reconstruction (see text).

target waveform in both trigger time and overall shape. Importantly, the frequency-domain panels show that the denoised reconstructions track the ground-truth spectral envelope in the analysis band, while the raw noisy traces exhibit excess stochastic power. Except for some weak features observed close to the low-frequency edge (~ 50 MHz), the denoiser tends to suppress incoherent power without introducing narrow-band artifacts. This behavior is directly relevant for reconstruction pipelines, which typically retain only antennas whose pulse candidates pass an SNR-based selection. See, for example, Ref. [36] and references therein.

A. Timing and peak-amplitude reconstruction accuracy

Here we evaluate the two quantities that enter radio fits most directly: the pulse arrival time (for UHECR direction reconstruction) and the peak amplitude (for energy-sensitive observables). In practice, reconstruction pipelines do not use all the detection units in the array indiscriminately. For a certain observed event, antennas are typically retained only if a pulse candidate exceeds an SNR threshold. We mirror this operational setting by restricting the following tests to *trigger-passing* traces. In particular, for each SNR bin we require the noisy pulse candidate to exceed a noise level estimate, $A_{\text{noisy}} \geq \sigma$,

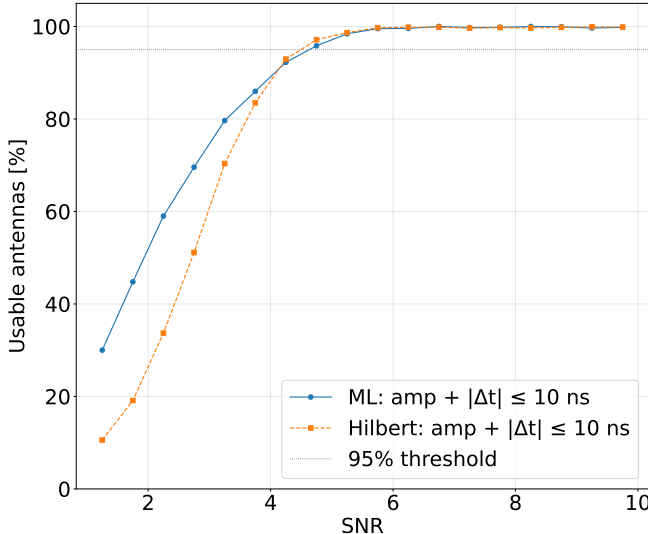


FIG. 8. Fraction of antennas meeting the direction-reconstruction quality cut (amplitude criterion plus $|\Delta t| \leq 10$ ns) as a function of SNR. The ML denoiser (solid) and the Hilbert-based baseline (dashed) converge for $\text{SNR} \gtrsim 4$, while the ML method retains a larger usable-antenna fraction at lower SNR. The horizontal dotted line marks the 95% usability threshold.

where A_{noisy} is the maximum of the Hilbert-transform envelope and σ is a noise scale estimated from the Hilbert envelope away from the signal window (under a Gaussian approximation).

We quantify timing performance with the denoising efficiency $\varepsilon(\tau)$, defined as the fraction of trigger-passing traces whose reconstructed peak time satisfies $|\Delta t_{\text{peak}}| \leq \tau$ relative to the clean peak time. We adopt $\tau = 10$ ns, a scale representative of the timing precision of the **Horizon Antenna** in the GRAND [26] experiment. Figure 6 shows $\varepsilon(10$ ns) as a function of SNR for each channel. The efficiency rises toward unity in the signal-dominated regime, indicating that the denoiser becomes effectively transparent when the pulse is already well resolved. The key gain for trigger time and amplitude reconstruction occurs at low-to-intermediate SNR. We note that without our denoising model, trigger time reconstruction is prone to catastrophic errors because the global maximum can be set by a random fluctuation and thus occur at an essentially arbitrary time. Hence, our ML denoising algorithm suppresses incoherent broadband contamination substantially increasing the fraction of reconstructed traces with $|\Delta t_{\text{peak}}| \leq 10$ ns.

In Fig. 7 we assess the pulse amplitude reconstruction using the peak-amplitude ratio $R_{\text{rec}} = A_{\text{rec}}/A_{\text{true}}$ for both the denoised output and the baseline estimate from the noisy trace. At low SNR, the baseline peak amplitudes show large scatter and a systematic tendency to overshoot. However, as the SNR increases, denoising stabilizes peak localization and suppresses incoherent power, driving R_{rec} toward unity. As expected, in the signal-

dominated regime, both the standard and ML approaches converge to $R_{\text{rec}} \simeq 1$. Together, these results show that denoising primarily improves the low-SNR regime that would otherwise be down-weighted or removed by standard quality cuts used in UHECR analyses [5].

B. Fraction of antennas meeting the direction-reconstruction quality cut

A first physics use case of denoised waveforms is UHECR direction reconstruction. In radio air-shower arrays, a UHECR direction estimate can be obtained by fitting a planar wavefront to antenna trigger times and positions. Such timing-based wavefront reconstruction is intrinsically sensitive to both timing outliers and the number of antennas (see, e.g., Refs. [34–37] for general discussions of wavefront/timing fits in radio arrays). Operationally, experiments therefore exclude unreliable antennas from the event fit.

Since UHECR direction reconstruction hinges on assigning reliable trigger times across many stations, we introduce a timing-grade antenna usability criterion. In particular, for each trace we extract a pulse time and peak amplitude from the Hilbert envelope, maximizing the envelope over the three polarizations and identifying the global envelope maximum. An antenna is deemed usable if (i) its reconstructed peak time is consistent with the clean reference within $|\Delta t_{\text{peak}}| \leq 10$ ns and (ii) its reconstructed peak envelope amplitude agrees with the clean value at the 25% level, $|A_{\text{rec}}/A_{\text{true}} - 1| \leq 0.25$.

Figure 8 displays the resulting usable-antenna fraction versus SNR for the ML denoiser and the Hilbert-envelope baseline. Two regimes are apparent. At $\text{SNR} \gtrsim 4$, both methods converge to near unity, indicating that when the pulse is signal-dominated the denoiser yields stable timing. In contrast, at $\text{SNR} \lesssim 4$ the ML denoiser retains a larger fraction of timing-grade antennas.

Because direction fits improve rapidly with increased number of triggered antennas, the gain in Fig. 8 directly translates into more stable and better-constrained wavefront fits. This is particularly important near threshold, where SNR-based antenna selection is most aggressive.

C. Physics-grade usable antennas: timing and waveform fidelity

While arrival direction is largely determined by the subset of antennas with robust pulse timing, energy-sensitive reconstruction additionally requires that denoising not distort the band-limited signal content used by amplitude and fluence based estimators. The latter are constructed from the waveform after conditioning to the experiment’s analysis band, which for GRAND is typically taken to be 50–200 MHz. We therefore classify an antenna as *physics-grade usable* if it satisfies the timing and peak-amplitude quality cuts defined above and, in

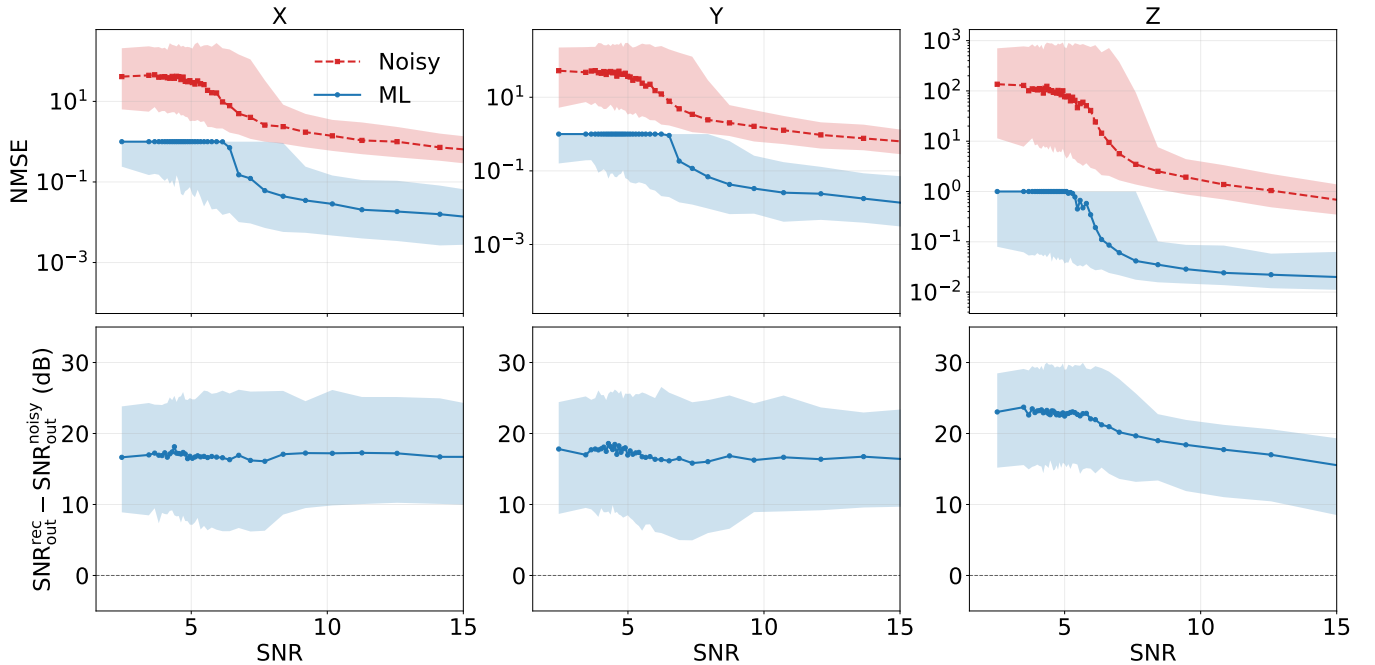


FIG. 9. **Reconstruction performance versus SNR for the three polarization channels (X, Y, Z).** *Top row:* normalized mean-squared error (NMSE) for the ML denoiser (blue) and the standard Hilbert-based method (red), evaluated in a signal-centered time window (see text). *Bottom row:* output-SNR improvement, $\Delta\text{SNR}_{\text{out}} \equiv \text{SNR}_{\text{out}}^{\text{rec}} - \text{SNR}_{\text{out}}^{\text{noisy}}$, computed in the same window (so the noisy baseline is $\Delta\text{SNR}_{\text{out}} = 0$). Curves show the medians across events, and shaded bands indicate the central 90% interval.

addition, passes a waveform-fidelity requirement evaluated in the same band and in a pulse-centered region of interest (ROI).

To quantify waveform fidelity in the regime relevant for energy-sensitive reconstruction, we compare reconstructed and reference ADC traces after applying the same band conditioning used in GRAND analyses, namely a band-pass to $\mathcal{B} = [50, 200]$ MHz [26]. We then restrict the comparison to a symmetric window of ± 150 ns about the true trigger time, so that the metric is dominated by the reconstructed pulse rather than by noise-only samples far from the signal. Within this ROI we compute a normalized mean-squared error,

$$\text{NMSE}_{\mathcal{B}} \equiv \frac{\sum_{t \in \text{ROI}} (x_{\text{rec}}^{\mathcal{B}}(t) - x_{\text{true}}^{\mathcal{B}}(t))^2}{\sum_{t \in \text{ROI}} (x_{\text{true}}^{\mathcal{B}}(t))^2}, \quad (10)$$

evaluated independently for each polarization channel.

Figure 9 summarizes the resulting waveform-level reconstruction quality as a function of SNR, shown separately for the three different polarizations. The top row displays the $\text{NMSE}_{\mathcal{B}}$ estimate for the ML denoiser and the Hilbert-based method. Across the full SNR range, the ML denoiser yields substantially lower $\text{NMSE}_{\mathcal{B}}$ than the standard method, with the largest separation in the noise-dominated regime. Even in the signal-dominated regime, the ML denoiser achieves systematically lower $\text{NMSE}_{\mathcal{B}}$ than the Hilbert-based baseline, indicating improved waveform fidelity across the full SNR range.

The bottom panels of Fig. 9 present the improvement in reconstructed output power computed in the same band-limited window, $\Delta\text{SNR}_{\text{out}} \equiv \text{SNR}_{\text{out}}^{\text{rec}} - \text{SNR}_{\text{out}}^{\text{noisy}}$. As can be seen, the denoiser produces a consistently positive gain, indicating that the reconstruction suppresses noise power in the band of interest without sacrificing the coherent pulse content. The trends are channel dependent, but the overall behavior is robust across polarizations.

To implement the waveform-fidelity requirement as a single quality cut, we impose $\text{NMSE}_{\mathcal{B}} \leq \text{NMSE}_{\text{max}}$ separately in each polarization channel. We fix this requirement once in the signal-dominated regime ($\text{SNR} \geq 6$) by choosing NMSE_{max} to yield a 95% pass rate for the baseline, and then apply this same threshold uniformly across SNR and for both methods. Figure 10 translates waveform fidelity into an effective number of usable antennas. It shows, as a function of SNR, the net increase in the number of antennas that satisfy the full physics-grade definition (timing, amplitude, and waveform fidelity) when using the ML denoiser instead of the Hilbert-based baseline. The gain is largest near the SNR threshold, where envelope-based peak picking can return plausible times while the underlying waveform is still appreciably contaminated. We also observe that the denoiser promotes a nontrivial subset of these marginal stations into the physics-grade category. At high SNR the difference becomes small because both methods recover waveforms that pass our waveform fidelity condi-

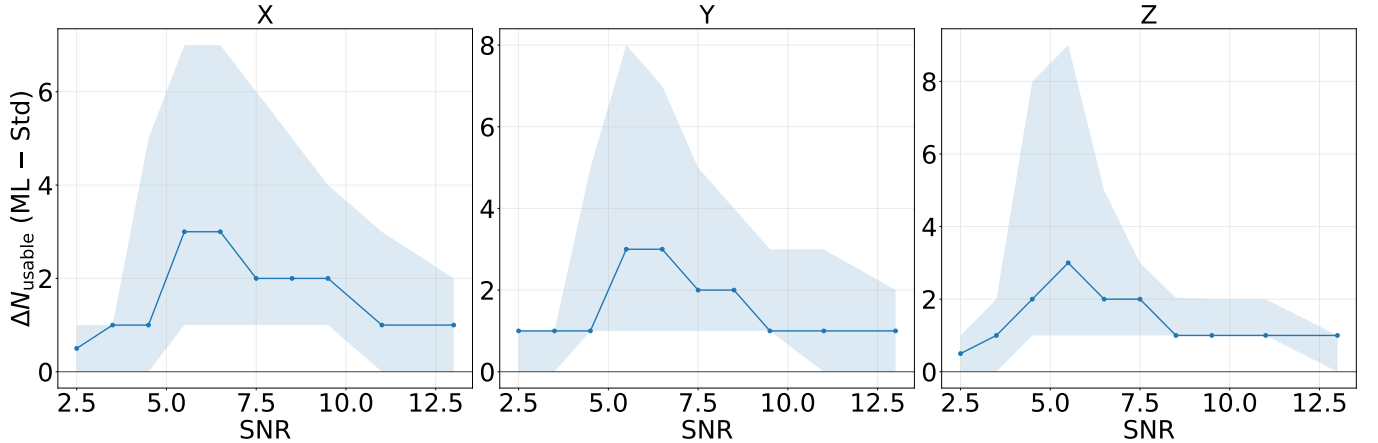


FIG. 10. **Gain in physics-grade usable antennas from the ML denoiser.** For each polarization (X, Y, Z) and SNR bin, we compute the event-by-event difference $\Delta N_{\text{usable}} \equiv N_{\text{usable}}^{\text{ML}} - N_{\text{usable}}^{\text{Hilbert}}$, where an antenna is counted as usable only if it passes the amplitude-quality requirement, satisfies $|\Delta t_{\text{peak}}| \leq 10$ ns, and meets the in-band waveform-fidelity cut in the 50–200 MHz analysis band. The solid curve shows the running median of ΔN_{usable} across events, and the shaded band encloses the central 68% interval (16th–84th percentiles).

tion. In a sparse radio array, this gain in the number of usable antennas can help stabilize downstream direction and energy fits, which are often limited by how many stations survive quality cuts.

D. Estimation of false-positive probability

To test whether the denoiser can hallucinate pulses, we apply it to signal-free time windows and count how often a full-trace scan would incorrectly flag a pulse. Because our simulation dataset does not include truly signal-free traces, we construct a noise-only dataset from the same simulations as follows: for each event we use the corresponding clean (noise-free) waveform to pinpoint the true pulse time, mask a conservative window around it, and then draw random off-pulse segments from the remaining parts of the noisy trace and stitch them into a full-length waveform. We then run the same full-trace scan on these constructed noise-only traces, where by definition, any flagged candidate is a false positive [38].

To make the comparison fair, we choose the pulse-candidate threshold directly from noise-only data, separately for each method (noisy input versus denoised output). Specifically, we tune the threshold so that, when we run the same full-trace scan on our constructed noise-only traces, only a fixed fraction are mistakenly flagged as containing a pulse. Throughout, we set this operating point to one false positive per 1,000 traces. With this false-positive budget fixed by construction, we then apply the identical scan to the signal-containing traces and measure, as a function of injected SNR, how often the true pulse is declared above threshold (the detection probability).

Figure 11 shows the detection probability as a function of injected SNR at a fixed operating point of one false

positive per thousand traces ($P_{\text{FP}} = 10^{-3}$). Each point is obtained by binning events in injected SNR and measuring the fraction whose pulse-candidate score exceeds the threshold calibrated from noise-only traces for each method respectively. We find that the denoiser curve lies above the noisy-input curve, meaning that at the same false-positive budget the denoiser recovers a larger fraction of real pulses, most noticeably in the low-to-moderate SNR regime where detection is marginal. Because the operating point is fixed using noise-only data for each method, this improvement reflects a genuine increase in separation between signal-present and noise-only cases after denoising.

V. DISCUSSION

For timing-based UHECR direction reconstruction in sparse radio arrays, denoising impacts performance primarily by increasing the number of stations that survive the timing-quality selection. In a planar-wavefront timing fit, the arrival direction is obtained from a regression over antenna positions and reconstructed peak times [34]. For fixed array geometry and approximately independent antenna timing errors, the corresponding pointing uncertainty scales approximately as

$$\sigma_{\theta} \propto \frac{\sigma_t}{\sqrt{N_{\text{use}}}}, \quad (11)$$

where N_{use} is the number of antennas retained after quality cuts and σ_t is the effective timing precision of those antennas. This scaling follows from the covariance of the planar-wavefront estimator and provides a useful proxy for interpreting changes in the number of stations [4].

Under the conservative assumption that all the retained antennas have a similar trigger time precision σ_t ,

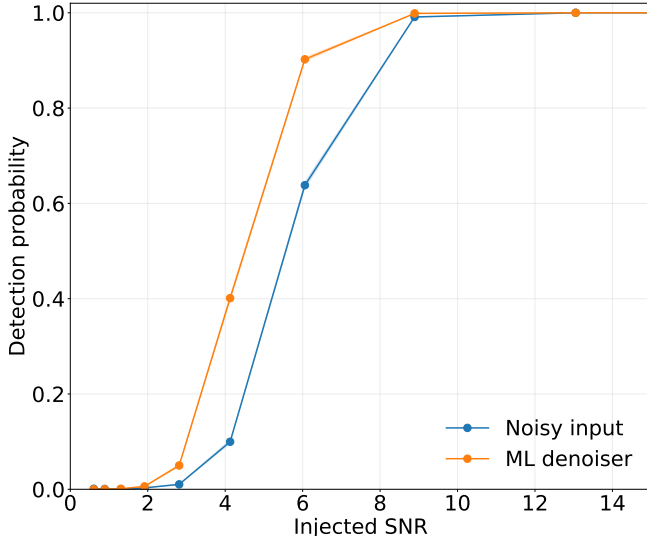


FIG. 11. **Detection probability versus injected SNR at fixed false-positive rate ($P_{\text{FP}} = 10^{-3}$).** Blue (orange) shows the pulse-candidate scan applied to the raw noisy (ML-denoised) traces. For each method, the scan threshold is calibrated on noise-only traces to enforce the same P_{FP} (see text).

the improvement in direction resolution could be estimated as

$$\frac{\sigma_{\theta}^{(\text{ML})}}{\sigma_{\theta}^{(\text{Hilbert})}} \simeq \sqrt{\frac{N_{\text{use}}^{(\text{Hilbert})}}{N_{\text{use}}^{(\text{ML})}}}. \quad (12)$$

Although our study is performed at the antenna level (without including event-level information), Fig. 8 can be used to gauge the potential size of this effect. In the low-SNR regime where denoising most strongly increases the retained fraction, we find $N_{\text{use}}^{(\text{ML})}/N_{\text{use}}^{(\text{Hilbert})} \sim 2\text{--}3$ around $\text{SNR} \simeq 1.5\text{--}2.5$, which would correspond to

$$\frac{\sigma_{\theta}^{(\text{ML})}}{\sigma_{\theta}^{(\text{Hilbert})}} \sim 0.6\text{--}0.75, \quad (13)$$

i.e. an approximate $\sim 25\text{--}40\%$ reduction in pointing uncertainty in this near-threshold regime. At high SNR, both approaches retain essentially all antennas, so any direction improvement coming from a larger number of usable antennas becomes negligible.

Importantly, we note that a denoiser method that recovers an accurate envelope peak and a plausible trigger time does not necessarily preserve the spectral content needed to reconstruct energy-sensitive observables. The *antenna usability* criteria introduced in Sec. IV C makes this distinction explicit by requiring waveform reconstruction fidelity in the frequency band of interest 50–200 MHz. With this requirement, the Hilbert-based baseline loses a significant fraction of antennas at low and intermediate SNR, while the ML denoiser continues to deliver waveforms that meet amplitude, timing, and spectral shape selection thresholds.

A practical concern with any ML denoiser is whether it can introduce spurious pulse candidates in pure noise. We address this directly by applying the same signal scan to noise-only traces (constructed from off-pulse windows) and choosing the scan threshold separately for the noisy input and the denoised output so that both methods satisfy the same fixed false-positive rate. In Fig. 11 we show that, at an identical false-positive budget, the ML denoiser achieves a higher detection probability. In practice, this means that genuine air-shower pulses are recovered more reliably, especially near threshold, without increasing the accepted fraction of noise-only traces under our stationary background model.

VI. CONCLUSIONS

We presented a convolutional denoising autoencoder trained on realistic simulated GRAND-like waveforms and evaluated it on an unseen test dataset. The model fuses time-domain and frequency-domain information to recover nanosecond-scale air-shower pulses in the presence of strong backgrounds. Quantitatively, the denoiser reduces the normalized mean squared error of the waveform by about an order of magnitude relative to a Hilbert-envelope baseline and yields a median output SNR improvement of $\sim 15\text{--}23$ dB. These waveform-level gains translate into operational improvements for GRAND-like reconstructions. In the low SNR regime ($\text{SNR} \simeq 1.5\text{--}2.5$) the fraction of antennas passing standard amplitude and $|\Delta t_{\text{peak}}| \leq 10$ ns timing selections increases by a factor of $\sim 2\text{--}3$, suggesting a $\sim 25\text{--}40\%$ reduction in timing-fit pointing uncertainty through the approximate $\sigma_{\theta} \propto 1/\sqrt{N_{\text{use}}}$ scaling. When we additionally require in-band waveform fidelity motivated by energy-sensitive observables, the denoiser promotes marginal stations to physics-grade, yielding a median increase of $\sim 3\text{--}4$ usable antennas around $\text{SNR} \simeq 5\text{--}6$ while becoming effectively transparent at higher SNR. Moreover, we explicitly quantified the risk of denoising-induced spurious pulse candidates by calibrating a fixed false-positive rate on noise-only windows and then measuring the resulting detection probability on signal-present traces. At the same false-positive budget, denoising improves near-threshold pulse recovery, indicating increased separation between noise-only and signal-present cases after denoising.

Finally, a natural next step is to embed the denoiser into an end-to-end GRAND reconstruction chain with the full detector response and more realistic, nonstationary backgrounds, and to propagate these antenna-level gains into event-level improvement in direction and energy resolutions.

DATA AND CODE AVAILABILITY

The code and analysis scripts to reproduce all figures are archived on Zenodo (DOI: [10.5281/zenodo.18233878](https://doi.org/10.5281/zenodo.18233878)) and are also available on GitHub ([grandmother/ML_denoising](https://github.com/grandmother/ML_denoising)). The clean waveforms are generated with ZHAIRES and the detector-response/noise model described in Sec. II. Additional data products are

available from the authors upon reasonable request.

ACKNOWLEDGMENTS

We thank Sara El Bouch, Claire Guépin, and Simon Prunet for fruitful discussions. We also thank the GRAND Collaboration for supplying *GRANDproto300* site parameters and related technical details used in this study. OM and ZL acknowledge support from the U.S. National Science Foundation under Grant No. 2418730.

[1] L. A. Anchordoqui, Ultra-High-Energy Cosmic Rays, *Phys. Rept.* **801**, 1 (2019), [arXiv:1807.09645 \[astro-ph.HE\]](https://arxiv.org/abs/1807.09645).

[2] M. Ahlers and F. Halzen, High-energy cosmic neutrino puzzle: a review, *Rept. Prog. Phys.* **78**, 126901 (2015).

[3] R. Alves Batista, The Quest for the Origins of Ultra-High-Energy Cosmic Rays, in *28th European Cosmic Ray Symposium* (2024) [arXiv:2412.17201 \[astro-ph.HE\]](https://arxiv.org/abs/2412.17201).

[4] J. Álvarez-Muñiz *et al.* (GRAND), The Giant Radio Array for Neutrino Detection (GRAND): Science and Design, *Sci. China Phys. Mech. Astron.* **63**, 219501 (2020), [arXiv:1810.09994 \[astro-ph.HE\]](https://arxiv.org/abs/1810.09994).

[5] T. Huege, Radio detection of cosmic ray air showers in the digital era, *Phys. Rept.* **620**, 1 (2016), [arXiv:1601.07426 \[astro-ph.IM\]](https://arxiv.org/abs/1601.07426).

[6] F. G. Schröder, Radio detection of Cosmic-Ray Air Showers and High-Energy Neutrinos, *Prog. Part. Nucl. Phys.* **93**, 1 (2017), [arXiv:1607.08781 \[astro-ph.IM\]](https://arxiv.org/abs/1607.08781).

[7] D. Shipilov, P. Bezyazeev, N. Budnev, D. Chernykh, O. Fedorov, O. Gress, A. Haungs, R. Hiller, T. Huege, Y. Kazarina, M. Kleifges, E. Korosteleva, D. Kostunin, L. Kuzmichev, V. Lenok, N. Lubsandorzhiev, T. Marshalkina, R. Monkhoev, E. Osipova, A. Pakhorukov, L. Pankov, V. Prosin, F. Schröder, and A. Zagorodnikov, Signal recognition and background suppression by matched filters and neural networks for tunka-rex, *EPJ Web of Conferences* **216**, 02003 (2019).

[8] C. K. O. Watanabe, P. S. R. Diniz, T. Huege, and J. de Mello Neto, Denoising cosmic rays radio signal using Wavelets techniques, *PoS ICRC2021*, 260 (2021).

[9] J. A. Högbom, Aperture Synthesis with a Non-Regular Distribution of Interferometer Baselines, *A&AS* **15**, 417 (1974).

[10] A. Horneffer *et al.* (LOPES), LOPES: Detecting radio emission from cosmic ray air showers, *Proc. SPIE Int. Soc. Opt. Eng.* **5500**, 129 (2004), [arXiv:astro-ph/0409641](https://arxiv.org/abs/astro-ph/0409641).

[11] S. Martinelli, T. Huege, D. Ravignani, and H. Schoorlemmer, Quantifying energy fluence and its uncertainty for radio emission from particle cascades in the presence of noise (2025), [arXiv:2407.18654 \[astro-ph.IM\]](https://arxiv.org/abs/2407.18654).

[12] C. Gheller and F. Vazza, Convolutional deep denoising autoencoders for radio astronomical images, *Monthly Notices of the Royal Astronomical Society* **509**, 990–1009 (2021).

[13] M. Terris, A. Dabbech, C. Tang, and Y. Wiaux, Image reconstruction algorithms in radio interferometry: From handcrafted to learned regularization denoisers, *Monthly Notices of the Royal Astronomical Society* **518**, 604–622 (2022).

[14] L. Einig, J. Pety, A. Roueff, P. Vandame, J. Chanussot, M. Gerin, J. H. Orkisz, P. Palud, M. G. Santa-Maria, V. de Souza Magalhaes, I. Bešlić, S. Bardeau, E. Bron, P. Chainais, J. R. Goicoechea, P. Gratier, V. V. Guzmán, A. Hughes, J. Kainulainen, D. Languignon, R. Lallent, F. Levrier, D. C. Lis, H. S. Liszt, J. Le Bourlot, F. Le Petit, K. Öberg, N. Peretto, E. Roueff, A. Sievers, P.-A. Thouvenin, and P. Tremblin, Deep learning denoising by dimension reduction: Application to the orion-b line cubes, *Astronomy & Astrophysics* **677**, A158 (2023).

[15] C. Reissel, S. Soni, M. Saleem, M. Coughlin, P. Harris, and E. Katsavounidis, Coherence deepclean: Toward autonomous denoising of gravitational-wave detector data, “” (2025), [arXiv:2501.04883 \[gr-qc\]](https://arxiv.org/abs/2501.04883).

[16] M. Erdmann, F. Schlüter, and R. Smida, Classification and Recovery of Radio Signals from Cosmic Ray Induced Air Showers with Deep Learning, *JINST* **14** (04), P04005, [arXiv:1901.04079 \[astro-ph.IM\]](https://arxiv.org/abs/1901.04079).

[17] P. Bezyazeev, D. Shipilov, D. Kostunin, I. Plokikh, A. Mikhaylenko, P. Turishcheva, S. Golovachev, V. Sotnikov, and E. Sotnikova, Reconstruction of sub-threshold events of cosmic-ray radio detectors using an autoencoder, in *Proceedings of 37th International Cosmic Ray Conference — PoS(ICRC2021)*, ICRC2021 (Sissa Medialab, 2021) p. 223.

[18] F. G. Schroeder and A. Rehman (IceCube), Application of Machine Learning to Identify Radio Pulses of Air Showers at the South Pole (ARENA 2024), *PoS ARENA2024*, 034 (2024), [arXiv:2502.19931 \[astro-ph.IM\]](https://arxiv.org/abs/2502.19931).

[19] R. Abbasi *et al.* (IceCube), Identification and Denoising of Radio Signals from Cosmic-Ray Air Showers using Convolutional Neural Networks, “” (2025), [arXiv:2508.14711 \[hep-ex\]](https://arxiv.org/abs/2508.14711).

[20] A. Benoit-Levy, Z. Lai, O. Macias, and A. Ferriere (GRAND), Denoising radio pulses from air showers using machine-learning methods, *PoS ICRC2025*, 185 (2025).

[21] P. Correa and J. Köhler (GRAND), NUTRIG: Development of a Novel Radio Self-Trigger for GRAND, *PoS ICRC2025*, 229 (2025), [arXiv:2507.04339 \[astro-ph.IM\]](https://arxiv.org/abs/2507.04339).

[22] S. Chiche, GRANDProto300: status, science case, and prospects (2024), [arXiv:2409.02195 \[astro-ph.HE\]](https://arxiv.org/abs/2409.02195).

[23] J. Alvarez-Muñiz, W. R. Carvalho, M. Tueros, and E. Zas, Coherent cherenkov radio pulses from hadronic

showers up to eev energies, *Astroparticle Physics* **35**, 287–299 (2012).

[24] C. S. C. Sanchez, P. M. Hansen, M. Tueros, J. Alvarez-Muñiz, and D. G. Melo, Uncertainties in the Estimation of Air Shower Observables from Monte Carlo Simulation of Radio Emission, (2025), arXiv:2505.08920 [astro-ph.HE].

[25] M. Guelfand (GRAND), The Giant Radio Array for Neutrino Detection (GRAND) and its prototype phases, in *58th Rencontres de Moriond on Very High Energy Phenomena in the Universe* (2025) arXiv:2501.01851 [astro-ph.IM].

[26] R. Alves Batista *et al.* (GRAND), GRANDlib: A simulation pipeline for the Giant Radio Array for Neutrino Detection (GRAND), *Comput. Phys. Commun.* **308**, 109461 (2025), arXiv:2408.10926 [astro-ph.IM].

[27] P. Vincent, H. Larochelle, Y. Bengio, and P.-A. Manzagol, Extracting and composing robust features with denoising autoencoders, in *Proceedings of the 25th International Conference on Machine Learning*, ACM International Conference Proceeding Series, Vol. 307 (ACM, 2008) pp. 1096–1103.

[28] K. He, X. Zhang, S. Ren, and J. Sun, *Identity mappings in deep residual networks* (2016), arXiv:1603.05027 [cs.CV].

[29] A. Paszke, S. Gross, F. Massa, A. Lerer, J. Bradbury, G. Chanan, T. Killeen, Z. Lin, N. Gimelshein, L. Antiga, A. Desmaison, A. Köpf, E. Yang, Z. DeVito, M. Raison, A. Tejani, S. Chilamkurthy, B. Steiner, L. Fang, J. Bai, and S. Chintala, *Pytorch: An imperative style, high-performance deep learning library* (2019), arXiv:1912.01703 [cs.LG].

[30] D. P. Kingma and J. Ba, *Adam: A method for stochastic optimization* (2017), arXiv:1412.6980 [cs.LG].

[31] L. N. Smith, *Cyclical learning rates for training neural networks* (2017), arXiv:1506.01186 [cs.CV].

[32] R. Liaw, E. Liang, R. Nishihara, P. Moritz, J. E. Gonzalez, and I. Stoica, *Tune: A research platform for distributed model selection and training* (2018), arXiv:1807.05118 [cs.LG].

[33] L. Li, K. Jamieson, A. Rostamizadeh, E. Gonina, M. Hardt, B. Recht, and A. Talwalkar, *A system for massively parallel hyperparameter tuning* (2020), arXiv:1810.05934 [cs.LG].

[34] A. Ferrière, S. Prunet, A. Benoit-Lévy, M. Guelfand, K. Kotera, and M. Tueros, Analytical planar wavefront reconstruction and error estimates for radio detection of extensive air showers, *Nuclear Instruments and Methods in Physics Research Section A: Accelerators, Spectrometers, Detectors and Associated Equipment* **1072**, 170178 (2025).

[35] O. Macias, Z. Mason, M. Ho, A. Ferrière, A. Benoit-Lévy, and M. Tueros, Simulation-Based Inference for Direction Reconstruction of Ultra-High-Energy Cosmic Rays with Radio Arrays, (2025), arXiv:2508.15991 [astro-ph.HE].

[36] V. Decoene, O. Martineau-Huynh, M. Tueros, and S. Chiche, A reconstruction procedure for very inclined extensive air showers based on radio signals, *Pos ICRC2021*, 211 (2021), arXiv:2107.03206 [astro-ph.IM].

[37] M. Guelfand, V. Decoene, O. Martineau-Huynh, S. Prunet, M. Tueros, O. Macias, and A. Benoit-Lévy, Reconstruction of inclined extensive air showers using radio signals: From arrival times and amplitudes to direction and energy, *Astropart. Phys.* **171**, 103120 (2025), arXiv:2504.18257 [astro-ph.HE].

[38] H. L. Van Trees, *Detection, Estimation, and Modulation Theory, Part I: Detection, Estimation, and Filtering Theory*, 2nd ed. (Wiley, New York, 2002).

Appendix A: Autoencoder architecture

We use a convolutional denoising autoencoder [27] to map a noisy three polarization trace $X \in \mathbb{R}^{3 \times 1024}$ to a denoised reconstruction \hat{X} . The encoder has parallel time and frequency pathways and a shared decoder back to the time domain.

1. Encoder

The time pathway applies an initial Conv1D($3 \rightarrow 16, k = 5, \text{stride} = 1, \text{pad} = 2$) with ReLU, followed by two residual blocks [28] with channel widths (32, 64). Max pooling (kernel 2, stride 2) follows the initial convolution and each residual block, yielding a time feature map $T \in \mathbb{R}^{64 \times 128}$.

The frequency pathway operates on the channelwise FFT of the input and processes magnitude and phase in two parallel sub branches that mirror the time pathway. After matching the downsampled frequency length to 128, the frequency features are combined to form $F \in \mathbb{R}^{64 \times 128}$.

We concatenate T and F along channels and apply a 1×1 fusion convolution to obtain the latent code $Z \in \mathbb{R}^{128 \times 128}$.

2. Decoder

The decoder maps Z to $\hat{X} \in \mathbb{R}^{3 \times 1024}$ using three transpose convolutions (kernel 4, stride 2, pad 1) with ReLU after the first two layers and a channel schedule ($128 \rightarrow 64 \rightarrow 32 \rightarrow 3$). The output layer is linear.

Appendix B: Training and validation

We implement the model in PyTorch [29] and optimize with Adam with weight decay [30]. We clip the gradient norm at 5 and checkpoint the epoch with the lowest validation loss. Learning rates follow a cyclical schedule (triangular or triangular2) with an 8 epoch period [31].

Hyperparameters are tuned with Ray Tune [32] using ASHA for early termination of underperforming trials [33]. We sample 64 configurations and train each for up to 50 epochs on a fixed train and validation split. We select the best configuration by validation loss, retrain once on train plus validation, and evaluate once on an untouched test set.

TABLE II. RayTune hyperparameter configuration for tuning the denoising network.

Parameter	Search Space
First Conv Channels (Time / Freq)	16, 32, 64
Residual Channels (Time / Freq)	(16, 32), (32, 64), (64, 128), (128, 256)
Decoder Channels	(256, 128, 64, 3), (128, 64, 32, 3), (64, 32, 16, 3), (32, 16, 8, 3)
Base Learning Rate	Log-uniform in $[10^{-6}, 10^{-3}]$
Max Learning Rate	Log-uniform in $[10^{-5}, 10^{-3}]$
Batch Size	{32, 64, 128}
Weight Decay	Log-uniform in $[10^{-5}, 5 \cdot 10^{-3}]$
Magnitude Weight	Log-uniform in $[10^{-2}, 1.0]$
Phase Weight	Log-uniform in $[10^{-2}, 1.0]$
Learning Rate Mode	{triangular, triangular2}

Appendix C: Ablation study

In order to obtain the most adequate training objective for the baseline, we performed a targeted ablation in which we keep the autoencoder architecture and training procedure fixed and vary only the loss function. In particular, we considered a purely mean-square error (MSE) time-domain objective such as,

$$L_{\text{MSE}} = \frac{1}{N} \sum_t \left[X(t) - \hat{X}(t) \right]^2, \quad (\text{C1})$$

and then tested extensions that explicitly enforce agreement not only in the reconstructed waveform, but also in its spectral magnitude and phase,

$$L_{\text{mag-MSE}} = \frac{1}{N_f} \sum_f \left(|X_f| - |\hat{X}_f| \right)^2, \quad (\text{C2a})$$

$$L_{\text{phase-MSE}} = \frac{1}{N_f} \sum_f \left(\arg \tilde{X}(f) - \arg \hat{X}(f) \right)^2, \quad (\text{C2b})$$

$$L_{\text{Multi-MSE}} = L_{\text{MSE}} + \sigma_{\text{mag-MSE}} L_{\text{mag-MSE}} + \sigma_{\text{phase-MSE}} L_{\text{phase-MSE}}. \quad (\text{C2c})$$

We also tested a purely mean-absolute error (MAE) or L1 time-domain objective,

$$L_{\text{L1}} = \frac{1}{N} \sum_t \left| X(t) - \hat{X}(t) \right|, \quad (\text{C3})$$

as well as extensions designed to enforce consistency across the signal's waveform, spectral magnitude, and phase.

$$L_{\text{mag-L1}} = \frac{1}{N_f} \sum_f \left| |X_f| - |\hat{X}_f| \right|, \quad (\text{C4a})$$

$$L_{\text{phase-L1}} = \frac{1}{N_f} \sum_f \left| \arg \tilde{X}(f) - \arg \hat{X}(f) \right|, \quad (\text{C4b})$$

$$L_{\text{Multi-L1}} = L_{\text{L1}} + \sigma_{\text{mag-L1}} L_{\text{mag-L1}} + \sigma_{\text{phase-L1}} L_{\text{phase-L1}}. \quad (\text{C4c})$$

The high and low SNR traces examples of the Multi-MSE and Multi-L1 objective functions are shown in Figure 12 and Figure 13.

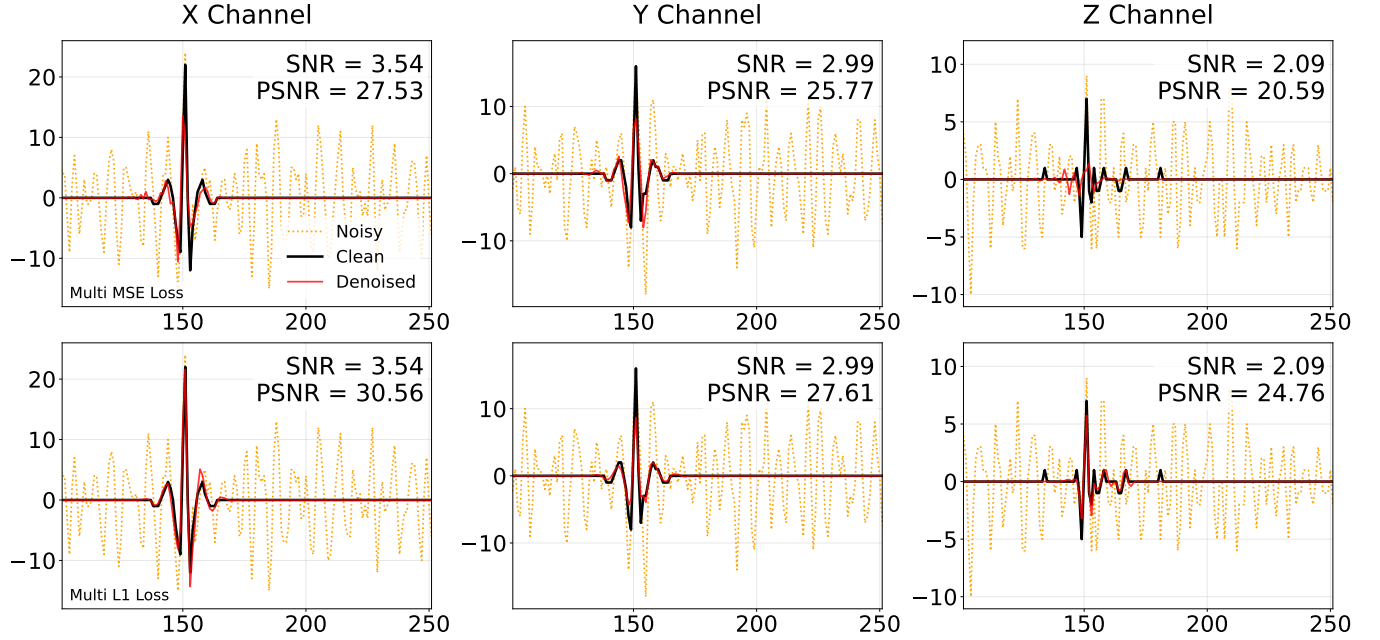


FIG. 12. **Comparison of denoising performance using Multi-MSE and Multi-L1 loss functions in the training.** Each panel displays a representative trace at low SNR. The first row corresponds to Multi-MSE (see Eq. C2), and the second row is the Multi-L1 (see Eq. C4), and each column represents a different polarization channel. The traces show the noisy input (orange, dashed), clean reference signal (black, solid), and denoised output (red, solid).

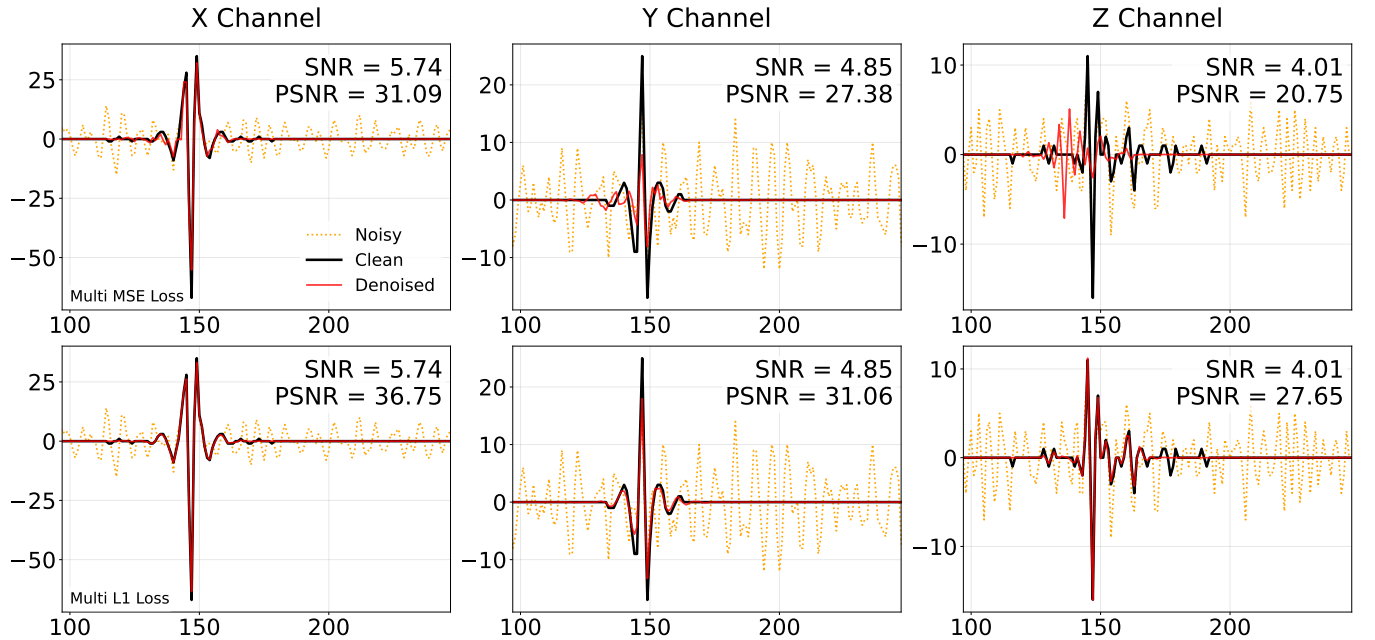


FIG. 13. Same as Fig. 12, except that this shows examples with medium SNRs.